Contents lists available at ScienceDirect

Journal of Wind Engineering & Industrial Aerodynamics

journal homepage: http://ees.elsevier.com

Numerical study of the effect of surface grooves on the aerodynamic performance of a NACA 4415 airfoil for small wind turbines

Yue Liu [a], Peifeng Li [b], Wei He [c], Kaiyong Jiang [a,*]

[a] Fujian Key Laboratory of Special Energy Manufacturing, Huaqiao University, Fujian, China
[b] James Watt School of Engineering, University of Glasgow, Glasgow, United Kingdom
[c] School of Engineering, University of Liverpool, Liverpool, United Kingdom

ARTICLE INFO

Keywords
Airfoil aerodynamics
Surface grooves
Flow separation
Small wind turbines
Computational fluid dynamics

ABSTRACT

Indented surface grooves can eliminate the laminar separation bubbles formed on airfoil surfaces, and thus have the potential to improve the aerodynamic performance of small wind turbines. In this study, a three-equation transitional turbulence model was selected and validated with experimental data to simulate the 2D flow around a NACA 4415 airfoil. Parametric simulation of surface groove characteristics was then conducted to investigate their effects on aerodynamic behavior. It was found that the recess depth ratio (h/δ, h: groove recess depth, δ: baseline boundary layer thickness) is the key influencing factor among the groove feature parameters, with the most effective value between $h/\delta = 1.0$ and 1.5. A smaller aspect ratio of recess depth to groove width is required to trap the vortex for a shallow recess depth, while a higher aspect ratio can stabilize the vortex for a deep recess. The endpoint of a groove can affect the potential vortex size within it, and the optimum endpoint is located around $0.16c$ (c: airfoil chord). Moreover, a rectangular groove especially for a recess depth ratio $h/\delta = 1.2 - 1.5$ offers better aerodynamic performance than an arc groove, as the rectangular configuration more efficiently restricts the flow motion inside the groove.

1. Introduction

The use of large scale wind turbine farms has led to tremendous growth in wind power capacity since the 90s. Large wind turbines (LWTs) are usually installed onshore or offshore, away from residence zones as they need ample space and may have some environmental impact such as noise pollution, landscape, and visual effect (Wang and Wang, 2015). Although LWTs can provide a high power generation capacity, the potential impact on climate conditions limits the expansion of LWTs (Wang and Prinn, 2010). An alternative scheme to meet increasing power demand without substantial side-effects is to employ decentralized small wind turbines (SWTs) (Tummala et al., 2016).

SWTs operate at lower Reynolds numbers compared to traditional LWTs as they have smaller rotor swept areas. Smaller blade size and the corresponding chord length (c) result in a lower Reynolds number based on chord Re_c ranging from 10^4 to 5×10^5. The formation of laminar separation bubbles (LSBs) can appear in this specific Re_c region. Laminar separation, transition, and reattachment occur within a short distance and dramatically affect the performance of the lifting surface (Gad-el-Hak, 1990), increasing drag, reducing aerodynamic efficiency, and thus degrading the performance of SWTs at some angles of attack ($AOAs$) (McTavish et al., 2013). Moreover, the sensitivity of LSBs to flow parameters (O'Meara and Mueller, 1987) causes a considerable uncertainty in the performance of SWTs, which are often subjected to turbulence, wind shear, wind shift and wind gust in service.

One essential characteristic of LSBs is the instability of the shear layers and the consequently unsteady behavior of the boundary layer. A small-amplitude natural disturbance could lead to separation shear layer roll-up and shedding vortex at a fundamental frequency, which then merges into the large vortex as the flow travels to the trailing edge (Kirk and Yarusevych, 2017). This large scale vortex shedding from the shear layer could bring oscillation and dynamic structural loading on the blade. In addition to the adverse effect of LSBs on aerodynamics, LSB formation has a significant impact on the airfoil aero-acoustics. Pröbsting and Yarusevych (2015) experimentally studied the tonal noise emission in LSBs. The vortex shedding from the separation bubbles would pass the trailing edge and generate tonal noise if the bubbles do not break up upstream.

Either a passive or active method could be implemented in order to control and eliminate LSBs. An active control method usually requires an extra energy supplier and a supplementary control system, which would increase the complexity of the entire system and usually incur a maintenance cost (Jamieson et al., 1992). A passive control method

* Corresponding author.
E-mail address: jiangky@hqu.edu.cn (K. Jiang)

https://doi.org/10.1016/j.jweia.2020.104263
Received 24 January 2020; Received in revised form 16 May 2020; Accepted 30 May 2020
Available online xxx
0167-6105/

is generally easy to use and brings less side effect on the original system. Traditional passive approaches like trips (Leknys et al., 2018) and vortex generators (Manolesos and Voutsinas, 2015; Zhang et al., 2016) are protruded turbulators and may generate too much turbulence. This would be a problem in the application of SWTs, as the different conditions of atmospheric stability should be an essential design aspect (Bukala et al., 2015). Indentations or grooves on the airfoil surface can potentially overcome this shortcoming and achieve the expected control purpose with less adverse effect. Early studies confirmed that dimpled balls (golf balls) travel a greater distance and have better control than smooth balls, and that dimple depth and shape have a decisive impact on the ball's aerodynamic properties (Davies, 1949). Recent experimental work related aerodynamic drag of golf balls to dimple size and configuration, and revealed the critical role of dimple depth and shape (Alam et al., 2011; Ting, 2003).

Despite the successful use of dimples on balls, their effect on the aerodynamics of airfoils is not yet clear. Robarge et al. (2004) replaced a closely spaced spanwise array of dimples by a two-dimensional (2D) groove and achieved minimal pressure losses and most effective flow separation control in an airfoil. The 2D groove designed with a particular geometry and position eliminates or postpones LSBs, but does not reduce drag. Seo and Hong (2016) subsequently performed a more detailed CFD simulation on the effect of groove size and position, and improved the lift-to-drag ratio by 15.3%.

Although round grooves could control LSB formation on an airfoil and reduce aerodynamic drag, the effectiveness of other types of crossprofiles (i.e., cross sections) is not clear. Moreover, there might be unavoidable inconsistencies between a designed arc groove and an actual manufactured one. A rectangular (rec) groove could be considered as a special case with the sharpest groove corner, while the arc groove has the roundest profile. Furthermore, the sensitivity to groove position cannot be neglected as SWTs are mainly used in uncertain environments.

In this paper, the flow around a NACA 4415 airfoil involving LSBs was simulated by solving the unsteady Reynolds-averaged Navier-Stokes (URANS) equations with two turbulence models $k-k_l-\omega$ and $Re_\theta-\gamma$, respectively. A high-fidelity transition model $k-k_l-\omega$ was used here to resolve the laminar separation and transition. A parametric simulation was then performed to investigate the effect of groove characteristics, including recess depth, aspect ratio, crossprofile, and groove position on the aerodynamic performance. The blade element method (BEM) was finally used to evaluate the effect of surface grooves on the service performance of a SWT using the airfoil.

2. Problem definition and numerical methods

2.1. Flow domain and groove geometry

The computational domain for the flow around the NACA 4415 airfoil is shown in Fig. 1. The flow was treated as two dimensional. The groove's geometry (crossprofile, recess depth h, width w) and position (endpoint) were simulated as a small 2D cavity under the static condition at $Re_c = 2\times10^5$ and $AOA = 10°$ (Fig. 1b). The selected $AOA = 10°$ is near the critical angle for the largest lift-to-drag ratio in this specific Re_c as SWTs are mainly designed to work under this condition to achieve the most efficient performance. The same inlet velocity conditions were set for the west, north and south boundaries. Pressure outlet conditions were set for the east boundary. No-slip boundary condition was imposed on the solid wall. The computational domain was divided into several blocks to generate a structured grid. Fig. 2 shows the generated grids in the computational domain and the details around the airfoil surface, in particular, the leading/trailing edges and the groove. Finer meshes were applied around the airfoil surface. The grid orthogonality was approximately attained near the airfoil surface to ensure calculation accuracy.

2.2. Governing equations and turbulence models

In the Re_c range involving LSB formation, the direct numerical simulation (DNS) is a straightforward method to predict transition and to understand the physics of the transition process. However, as the DNS solves the Navier-Stokes equations with the whole range of spatial and temporal scales, the computational cost is too high as the mesh resolution requirement for DNS is around the Kolmogorov scale ($x^+ = 3.4-8.3$, $y^+ = 0.5-1$, $z^+ = 5-18.9$ (Jones et al., 2018)). To overcome this obstacle, turbulence models are utilized. The URANS equations coupled with transition models provide an efficient way to simulate LSBs in 2D.

Lin and Sarlak (2016) compared $Re_\theta-\gamma$ and $k-k_l-\omega$ transition models with traditional $k-\omega$ SST model and concluded that $k-k_l-\omega$ model could better predict the flow before stall. Another work carried out by Wauters and Degroote (2018) compared a series of transitional turbulence models. According to their 2D study, the $Re_\theta-\gamma$, γ, and $k-k_l-\omega$ models could give a good prediction in the lower-AOA region.

In this paper, the URANS equations were coupled with two different turbulent transition models: $Re_\theta-\gamma$ (Langtry and Menter, 2009) and $k-k_l-\omega$ (Walters and Cokljat, 2008). The results were compared

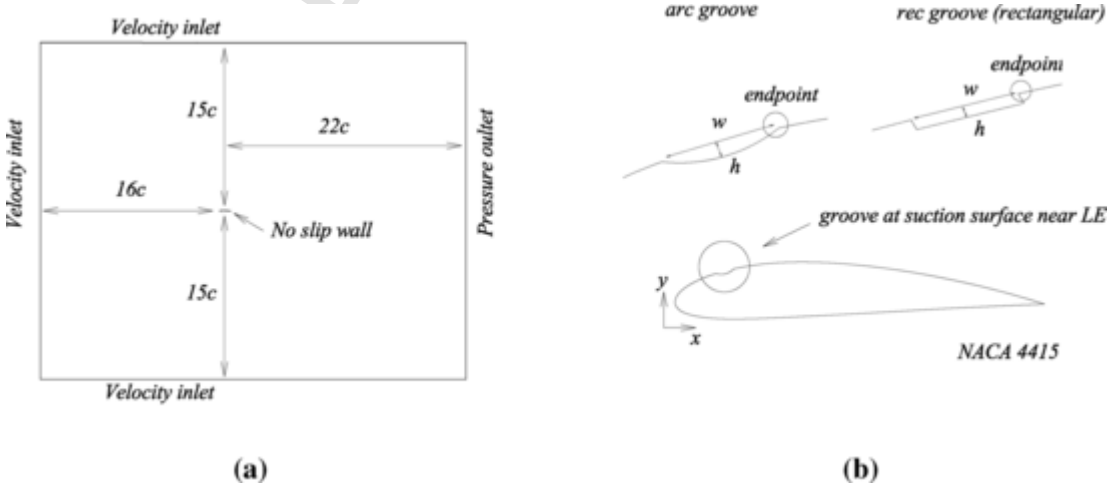

Fig. 1. (a) The 2D computational domain with boundary conditions, and (b) the groove on a NACA 4415 airfoil surface.

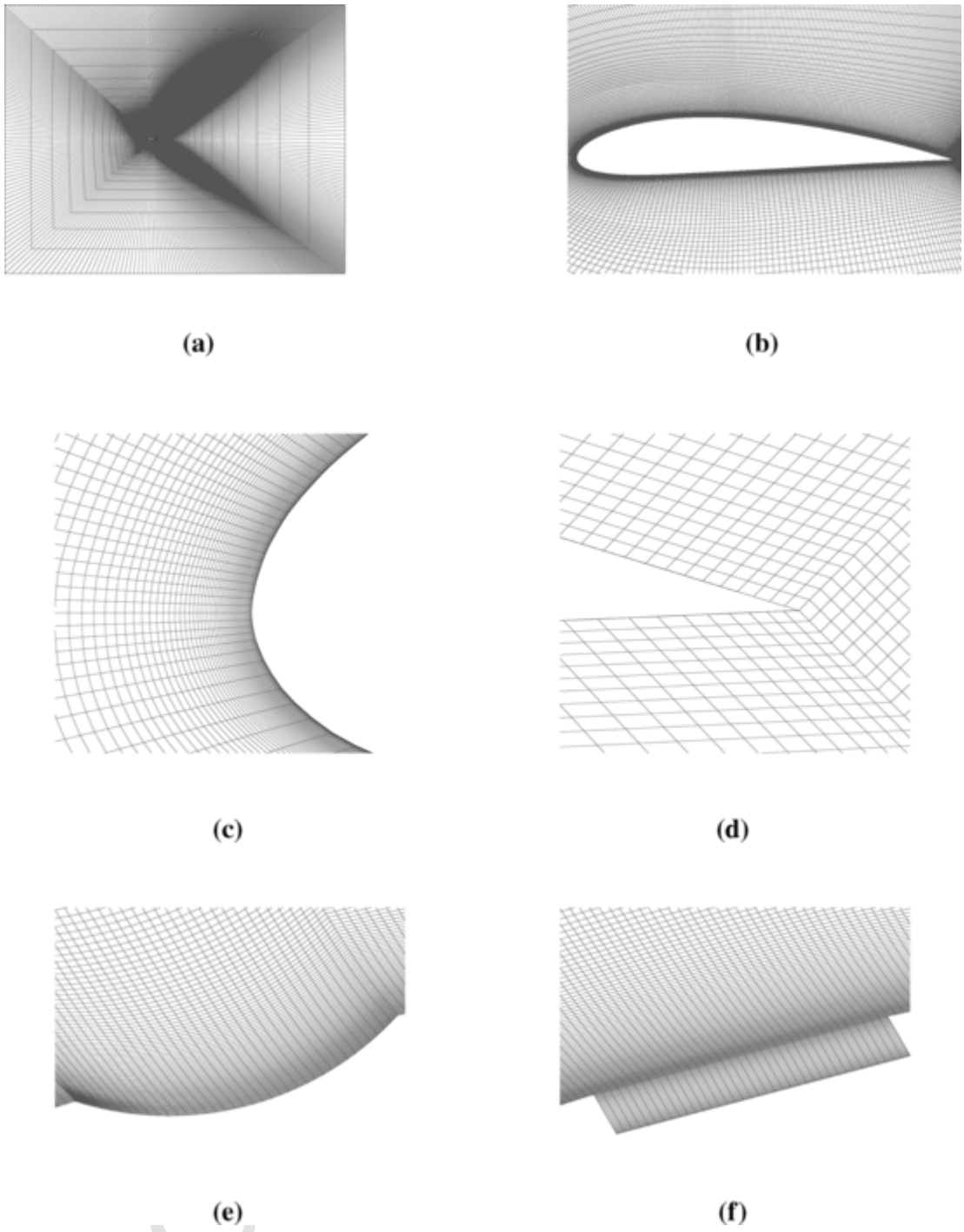

Fig. 2. Details of the grids (a) in the computational domain, (b) around the airfoil surface, (c, d) around the leading and trailing edges, and (e, f) around the arc or rec groove.

with the experimental data of Saliveros, 1988. The $k-k_l-\omega$ model was finally chosen to simulate the problem as its predictions were more accurate in the specific condition.

2.3. Inflow conditions

Among all those inflow conditions, the turbulence intensity (Tu) seems to be a key factor. Saliveros, 1988 concluded that the Tu level between 0.02% and 0.2% is important whilst Tu>0.2% may have negligible effects. Devinant et al. (2002) suggested that the aerodynamic behavior of an airfoil can be strongly influenced by the turbulence level. Wafula et al. (2016) revealed that the inflow turbulence causes fluctuating aerodynamic loads on the turbine blade and ultimately affects the aerodynamic performance.

Another problem in the inflow conditions specifically arises in the RANS turbulence model, as it is crucial to apply the appropriate boundary conditions for the turbulence variables at distant boundaries. According to Spalart and Rumsey (2007), the coarse grid far from the body may result in an inaccurate computation, and the decay of turbulence quantities can be grossly underestimated. Thus, the turbulent inflow parameters Tu and the viscosity ratio should be carefully chosen. Table 1 lists the Tu level and viscosity ratio or turbulent length scale reported previously.

Table 1
URANS simulations with different transition models and inflow conditions.

References	Airfoil	$Re_c(10^5)$	$AOA(^\circ)$	Model	Tu(%)	Viscosity ratio	Turbulent length scale
Wauters et al. (2019)	NACA 0018	3	0–25	Low Re SST $Re_\theta - \gamma$ $\gamma - SST$ $k - k_l - \omega$	0.04	0.06	–
Zhang et al. (2017)	DU91-W2-250	10	−3–10	SST $k-\omega$ $k - k_l - \omega$	0.06	0.73	–
Choudhry et al. (2015)	NACA 0021	1.2	0–20	$Re_\theta - \gamma$ $k - k_l - \omega$	7.5	–	0.01
Fürst et al. (2013)	NACA 0012	6, 4, 2	0	$k - k_l - \omega$	0.3	8	–
Sanders et al. (2010a)	lightly loaded LPT	0.15–1	30.94	$k - k_l - \omega$	0.5–1.5	–	0.002–0.05
Sanders et al. (2010b)	highly loaded LPT	0.25, 0.5, 1	30.94	$k - k_l - \omega$	0.6	–	0.005, 0.05
Pacciani et al. (2011)	T106C, T108	0.5, 2.1	34.7	$k - k_l - \omega$	0.4, 4	0.0025	–
Reza et al. (2009)	S809	30	–	$k - k_l - \omega$	0.07	–	–
Walters and Cokljat (2008)	A-airfoil, S809	20	13.3, 0 - 20	$k - k_l - \omega$	0.2	10	–
Langtry et al. (2006)	S809	20	1, 9, 14, 20	$Re_\theta - \gamma$	0.2	–	–

Typically, an increasing viscosity ratio decreases the decay. In this paper, the large viscosity ratio used by Walters and Cokljat (2008) was compared to the small viscosity ratio recommended by Spalart and Rumsey (2007). Very rapid decay takes place with the small viscosity ratio in this Tu level and could not meet the condition in the experiment, so the large viscosity ratio was chosen in the model. The laminar kinetic energy k_l was set as $k_l = \frac{1}{3}k_\infty = \frac{1}{3}\cdot\frac{3}{2}U_\infty^2 Tu^2$ for the $k - k_l - \omega$ model (Mayle and Schulz, 1996).

2.4. Model validation

The simulation was performed in the Ansys Fluent finite volume method solver. The spatial discretization for the gradient term was least-squares cell-based, the pressure term was second order, and the momentum term was second-order upwind. The second-order implicit method was used for transient discretization. The PISO algorithm was used to solve the pressure-velocity coupling problem, and neighbor coupling was adopted to enhance convergence. The residual for all parameters was 10^{-5} as it can give sufficient accuracy in reasonable computational time. The nondimensional time step $\Delta t = \delta t U_\infty / c$ was tested with 0.001, 0.0005, and 0.0001. A smaller time step is needed to resolve the unsteady phenomenon in the boundary layer. Moreover, a small time step size is suitable for small spatial discretization. The time step size was 0.0005 for the simulation with a fixed $AOA = 10^\circ$ in this study.

Table 2
Predicted drag and lift coefficients with three different grid densities.

Index	Number of cells	Ns	Nr	C_d	C_l
#1-fine	462,747	1370	290	0.0305	1.3178
#2-medium	230,907	1010	200	0.0315	1.3177
#3-coarse	114,212	690	145	0.0321	1.3333
Saliveros, 1988	–	–	–	0.03	1.3

To study the grid dependency, the simulation was run with three different grid densities. The grid density was controlled by the total number of cells, the number of nodes along the airfoil surface (Ns) and the number of nodes along the radial direction away from the airfoil (Nr). The drag (C_d) and lift (C_l) coefficients were averaged using the fully developed flow between the nondimensional time $t = 50 - 100$, and then compared with the experimental data by Saliveros, 1988 as illustrated in Table 2. Fig. 3 compares the time-averaged pressure coefficient (C_p) and wall shear stress (τ_{wall-x}) predicted using the three grids. Both the fine and medium grid densities produce very similar simulation results. Considering the computational cost and accuracy, the medium grid density was finally chosen for the simulations. The predictions of C_d, C_l, C_p and τ_{wall-x} averaged between $t = 50 - 100$ are consistent with the predictions averaged between $t = 20 - 70$ in which the flow can also be considered to be fully developed. Therefore, in the subsequent analysis for the baseline airfoil and the airfoil with grooves, the nondimensional time $t = 20 - 70$ was used to average the predictions.

Fig. 4 compares the mean pressure coefficient between the models ($k - k_l - \omega$ and $Re_\theta - \gamma$) and the experimental data. Both models predict the mean pressure coefficient at the airfoil surface very well. The only inconsistency occurs at the transition where the $k - k_l - \omega$ model agrees slightly better with the experiments than the $Re_\theta - \gamma$ model. The

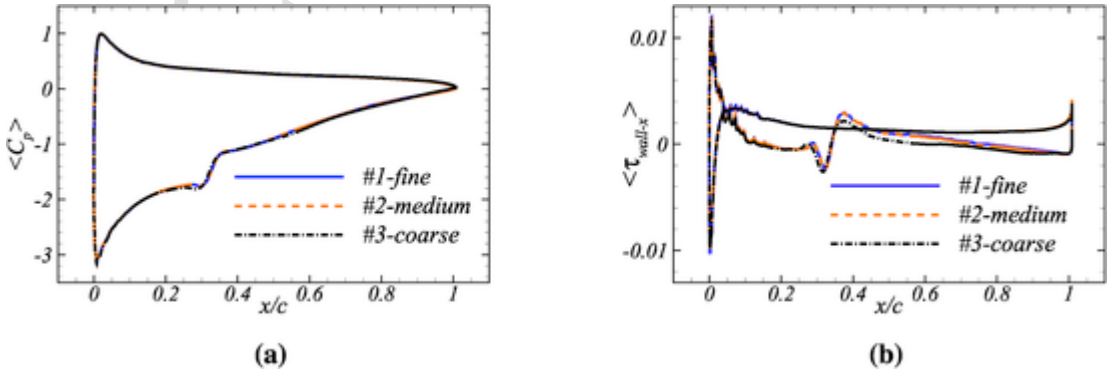

Fig. 3. Predicted mean values of (a) pressure coefficient C_p and (b) wall shear stress τ_{wall-x} with three different grid densities.

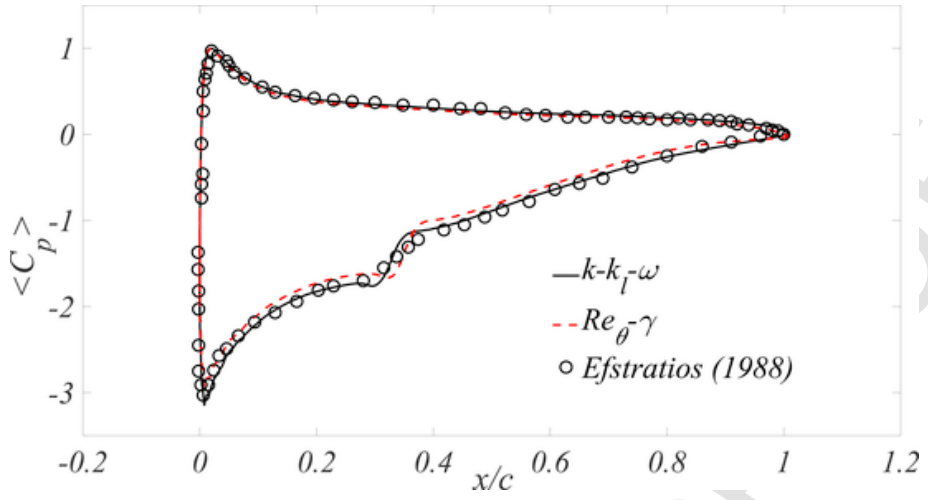

Fig. 4. Comparison of predicted mean Cp by the two models with the results of Saliveros, 1988.

$Re_\theta - \gamma$ model tends to predict the laminar separation and transition point backwardly. The first layer of the grid to the wall was set to $\Delta y = 10^{-4}c$ and $4 \times 10^{-5}c$ to study the dimensionless wall distance y^+ (calculated with local wall friction velocity) sensitivity. A wall-normal expansion ratio of 1.1 was utilized in both cases. Fig. 5 shows the y^+ and mean-C_p calculated along the airfoil upper surface with the two different Δy. The consistency of mean-C_p suggests that y^+<2 can give an accurate result.

3. Results and discussion

3.1. Aerodynamic characteristics of the baseline airfoil without grooves

Fig. 6a shows the simulation results of the transient vorticity and mean-flow streamlines in the baseline NACA 4415 airfoil without grooves. The results predict the formation of LSBs near the leading edge, vortex shedding on the separated shear layer and turbulent boundary layer separation at the trailing edge. This is consistent with the results of many researchers (Lin and Pauley, 1996; Kirk and Yarusevych, 2017).

The separation point in the boundary layer corresponds to the point of vanishing wall shear in this work. The time-averaged wall shear stress in the flow direction at the upper surface of the airfoil (Fig. 6b) was used to determine the laminar separation point (LSP), reattachment point (RAP) and turbulent boundary layer separation point (TSP). Table 3 gives the calculated separation and reattachment points which are compared with the experimental results of Saliveros, 1988. This baseline flow field provides the reference information to select surface groove parameters in order to control and eliminate the LSBs.

3.2. Groove parameters in the simulation

Various groove parameters were selected to investigate their effects on the aerodynamic performance of the airfoil (Table 4). According to Robarge et al. (2004), the optimum position to locate the groove is directly in front of the LSBs. The baseline endpoint for a groove was set at $x = 0.16c$ according to the baseline airfoil LSP in Table 3. The optimum ratio of recess depth (h) to reference pre-recess local boundary layer thickness (δ) is between $h/\delta = 0.6 - 1.0$ (Robarge et al., 2004). To examine the recess depth effect thoroughly, values of $h/\delta = 0.5 - 2.0$ were used in the simulations. The reference boundary layer thickness at LSP for the baseline case (without groove) is $\delta = 0.005c$. Five recess depth ratios (h/δ = 0.5, 1.0, 1.2, 1.5, 2.0) were chosen. The optimum aspect ratio of recess depth to groove width was $h/w = 0.1 - 0.15$. Furthermore, to investigate the effect of the crossprofile geometry on eliminating LSBs under the working conditions of SWTs, two common crossprofiles: arc and rectangular (rec) were simulated as they can be manufactured easily.

In the application of SWTs, the groove position relative to the LSPs is most likely to change during the operation under variable environments. The position effect of arc groove has been discussed by Seo and Hong (2016), but the shifting distance of the groove is so small that control effectiveness is not apparent. Moving the groove downstream and upstream compared to the reference position (endpoint $x = 0.16c$) with a distance relative to the groove width w, resulted in different endpoint positions (Table 4). The effect of groove position was simulated for the reference recess depth of $h/\delta = 1.2$.

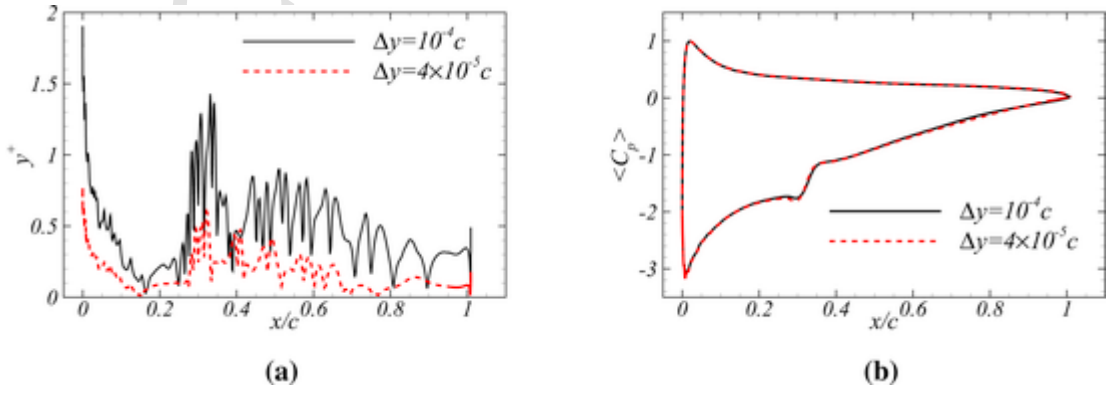

Fig. 5. Sensitivity study of (a) y^+ distribution and (b) mean-C_p to first layer distance Δy.

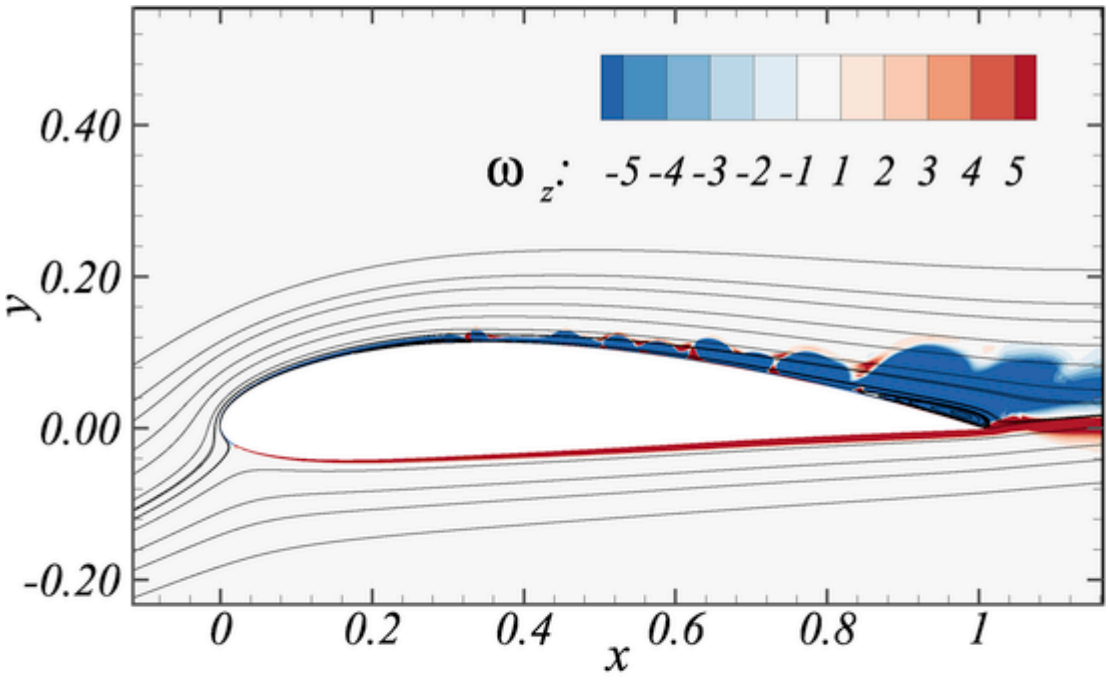

(a)

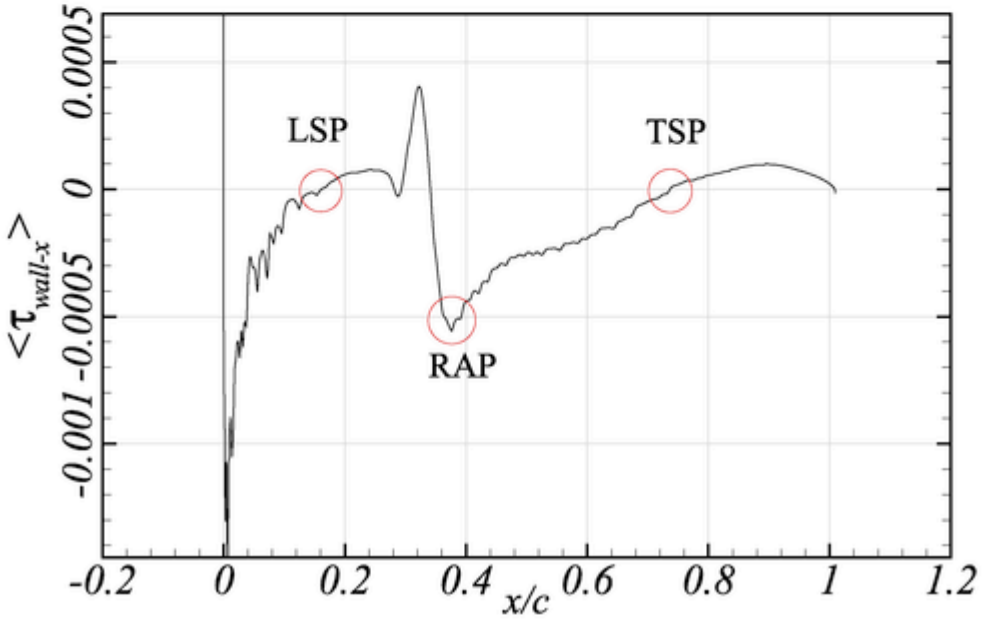

(b)

Fig. 6. (a) Distribution of instantaneous vorticity and mean streamlines, and (b) mean wall shear stress τ_{wall-x}, in the upper airfoil surface for $Re_c = 2 \times 10^5$ and $AOA = 10°$.

A relative lift-to-drag ratio $\Delta C_l/C_d$ was defined to quantify the effect of these groove parameters on the aerodynamic performance of the airfoil:

$$\Delta C_l/C_d = \frac{C_l/C_d - (C_l/C_d)_{baseline}}{(C_l/C_d)_{baseline}} \times 100\% \quad (1)$$

where $(C_l/C_d)_{baseline}$ is the lift-to-drag ratio in the baseline airfoil without grooves. An increased $\Delta C_l/C_d$ suggests improvement of the aerodynamic performance of the airfoil by surface grooves.

Table 3
Comparison of mean separation and reattachment points with experiment (Saliveros, 1988). Vis is the position from visualization and C_p that from pressure coefficient data.

AOA	Re_c		Experiment	Simulation	
			Vis	C_p	
10°	2×10^5	LSP	$0.1c$	$0.18c$	$0.16c$
		RAP	$0.345c$	$0.376c$	$0.34c$
		TSP	$0.7c$	–	$0.73c$

Table 4
Airfoil surface groove geometry and position in the simulation.

Parameters	Value
Recess depth ratio (h/δ)	0.5, 1.0, 1.2, 1.5, 2.0
Aspect ratio (h/w)	0.1, 0.15
Crossprofile	arc, rec
Endpoint position (x/c)	0.1, 0.12, 0.16, 0.18, 0.19, 0.2, 0.22

3.3. Effect of groove geometry

3.3.1. Recess depth effect

Fig. 7 shows the effect of groove geometry on the relative lift-to-drag ratio $\Delta C_l/C_d$. Of all the geometry parameters studied in this paper, the recess depth ratio plays a significant role in determining the controlling effectiveness. An increase of $\Delta C_l/C_d$ is achieved for the recess depth ratio from $h/\delta = 1.0$ to 1.5. However, the effect could be neglected for the shallowest condition ($h/\delta = 0.5$). A reduced $\Delta C_l/C_d$ is observed for the deepest condition ($h/\delta = 2.0$).

Fig. 8 demonstrates the mean-flow streamlines of three recess depth ratios ($h/\delta = 0.5$, 1.2 and 2.0) to give distinguishable features in the boundary layer. The $h/\delta = 0.5$ represents the case in which the shallowest groove has hardly any positive boundary layer controlling effect. As illustrated in Fig. 8a&b, the vortex formed inside the groove goes out of the downstream edge of the groove, especially for the rec geometry, causing unsteadiness and vortex shedding. For the recess depth ratio $h/\delta = 1.2$ (Fig. 8c&d), the vortex is completely trapped in the groove. For deep grooves with $h/\delta = 2.0$ (Fig. 8e&f), the vortex tends to form near the upstream edge of the groove, in particular, second vortices form in the vicinity of the corners of the rec groove. The formed vortex is prone to cause additional vortex shedding into the boundary layer. This may be harmful to the airfoil performance.

Fig. 9 shows the boundary layer velocity profile $\langle U_x \rangle$ at six locations of the upper surface: $x = 0.1c$ (before the groove), $0.16c$ (groove endpoint), $0.2c$, $0.4c$, $0.6c$ and $0.8c$ in the airfoil with and without a groove. At the locations near the groove ($x \leq 0.2c$), the velocity profile tends to deviate more from the baseline condition with increasing recess depth. This indicates that the recess depth can bring about direct influent disturbance to the boundary layer. For the downstream locations with the turbulent boundary layer ($x \geq 0.4c$), the velocity also deviates from the baseline case. However, the velocity increases more rapidly with the normal distance y for $h/\delta = 1.0$, 1.2 and 1.5 which has better aerodynamic performance (Fig. 7). This is probably because the turbulent boundary layer gains more kinetic energy to overcome separation near the trailing edge for the $h/\delta = 1.0$, 1.2 and 1.5. For the shallow groove $h/\delta = 0.5$, the velocity profile at each surface location almost coincides with the baseline profile. Thus, the recess depth h should be appropriately selected to modify turbulent boundary layer properties beneficially.

3.3.2. Aspect ratio effect

Fig. 10a shows the vortex structure in a groove with different aspect ratios for the recess depth ratio $h/\delta = 1.0$ and the arc crossprofile. The groove with an aspect ratio $h/w = 0.1$ traps the vortex, but an unsteady second vortex occurs near the bottom wall for $h/w = 0.15$. For the rec crossprofile (Fig. 10b), the aspect ratio $h/w = 0.1$ groove has the same controlling effect and traps the vortex, but in the aspect ratio $h/w = 0.15$ groove, the vortex spreads out of the groove like the situation occurring with a recess depth ratio $h/\delta = 0.5$ (Fig. 8b). Fig. 10c&d shows that the vortex forms near the downstream edge of the groove for $h/\delta = 1.5$.

The aspect ratio is not an independent factor but acts together with the recess depth to determine the size of the groove. A shallow groove requires a smaller aspect ratio (a wider groove) to allow the vortex to be better trapped but not spread out of the trailing edge of the groove (Fig. 10b). If the groove is deep, a larger aspect ratio with narrower groove width is required to ensure that the vortex does not oscillate in the groove and the boundary layer is steady (Fig. 10c). For the optimum recess depth ratio $h/\delta = 1.2$, increasing h/w from 0.1 to 0.15 leads

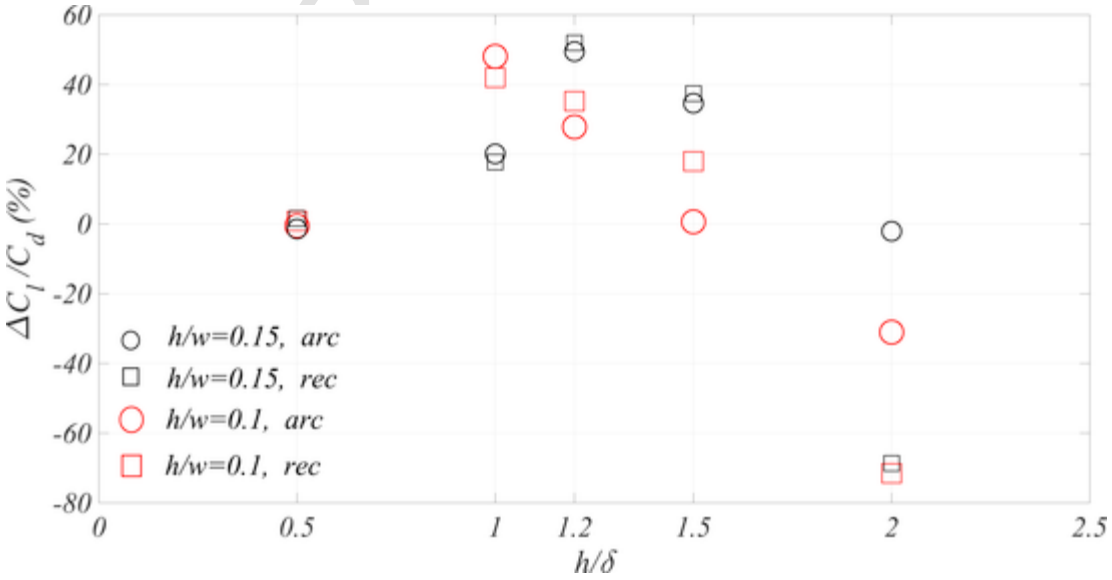

Fig. 7. The effect of groove geometry on the relative lift-to-drag ratio of the airfoil.

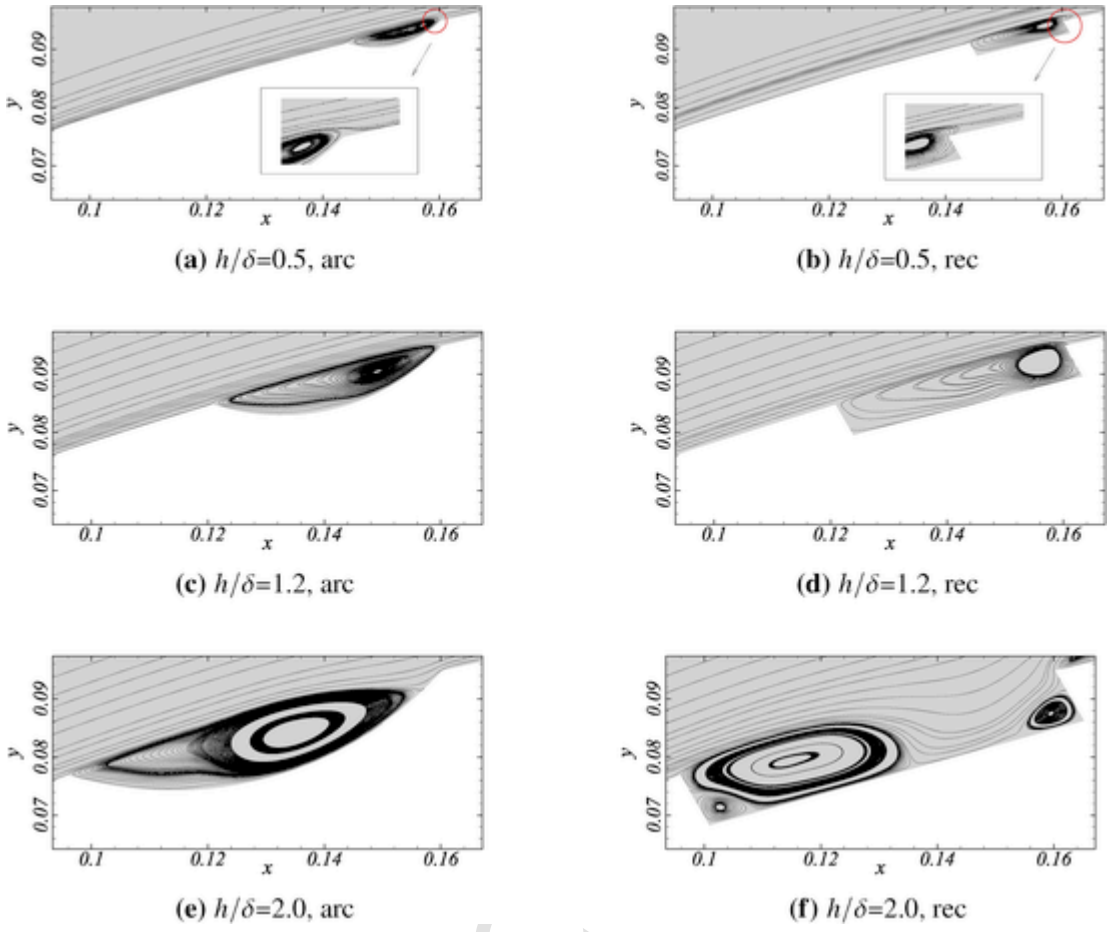

Fig. 8. The mean streamlines illustrating the fluid-structure around the airfoil with a groove of different recess depths ratio h/δ. The groove aspect ratio is $h/w = 0.15$.

to increased $\Delta C_l/C_d$ and, thus, better aerodynamic performance for both arc and rec grooves (Fig. 7).

3.3.3. Crossprofile effect

Compared to the size parameters (recess depth and aspect ratio), changing the crossprofile (cross section) might not cause a significant difference in the boundary layer. The most compelling cases with recess depth ratio $h/\delta = 1.2$ are chosen to explain the crossprofile effect. Fig. 11 shows the mean velocity vector in the groove with different h/w and crossprofiles. The distribution of the velocity vector is similar in the four cases. The velocity magnitude increases along the groove surface from the leading to trailing edge sides. With this recess depth ratio $h/\delta = 1.2$, the airfoil performs well as the recirculation zone occupies the groove to eliminate LSBs. To achieve the best controlling effect, the vortex should remain within the groove.

Fig. 11 also plots the boundary layer velocity profiles at seven positions around the groove and compares them with the baseline condition. The y coordinate of the baseline case at $\langle U_x \rangle = 0$ corresponds to the position outside of the groove. The velocity in the rec groove is lower than the velocity in the arc groove at the positions $x = 0.11c$ (near the leading edge), $x = 0.14c$ and $x = 0.15c$ (near the trailing edge). This might suggest that the rec groove more likely retards the fluid motion within it, especially around its corners. Furthermore, the variation of the velocity magnitude in the groove with different h/w and crossprofiles in Fig. 11 is similar to their effects on the $\Delta C_l/C_d$ (Fig. 7). Fig. 7 also illustrates that the rec crossrofile performs slightly better than the arc crossprofile for $h/\delta = 1.2$ to 1.5. Therefore, the rec groove reduces friction drag and stabilizes the trapped vortex more than the arc groove in these conditions.

3.4. Effect of groove position

Fig. 12 shows the groove position sensitivity of the relative lift-to-drag ratio for the optimum recess depth $h/\delta = 1.2$. For an arc or rec surface groove with an aspect ratio $h/w = 0.1$, the airfoil performs better as the groove moves downstream. The optimum position for the rec groove with $h/w = 0.15$ is at $x = 0.16c$.

Fig. 13 shows the instantaneous vorticity distribution at $t = 70$ and streamlines around the groove of each position. The column shows the results for the same groove size and crossprofile while the row shows the results with the same groove position. The reference case $x = 0.16c$ is shown in the first row of Fig. 13. The vortex is well trapped for all groove configurations in the reference case. The second and fourth rows illustrate that moving the groove downstream with a distance of one groove width and half a groove width, respectively, leads to an increase of the boundary layer thickness at the leading edge side of the groove. The vortex formed in the groove moving downstream is larger compared to the reference case. This is beneficial in the arc configuration but unfavorable for the rec crossprofile. The enlargement of the vortex consequently distorts the vortex structure as the groove is not large enough to accommodate it. It could trigger a second vortex near the vortex core (Fig. 13e,g,h,p). When the groove moves upstream (the third row in Fig. 13), the boundary layer becomes thinner. Small vortex forms in the groove and cannot occupy the whole groove space (Fig. 13i), leading to worse performance.

Therefore, the groove position affects the size of potential vortices formed within the groove and the local boundary layer thickness. The groove geometry should be adjusted to better trap the vortex. More-

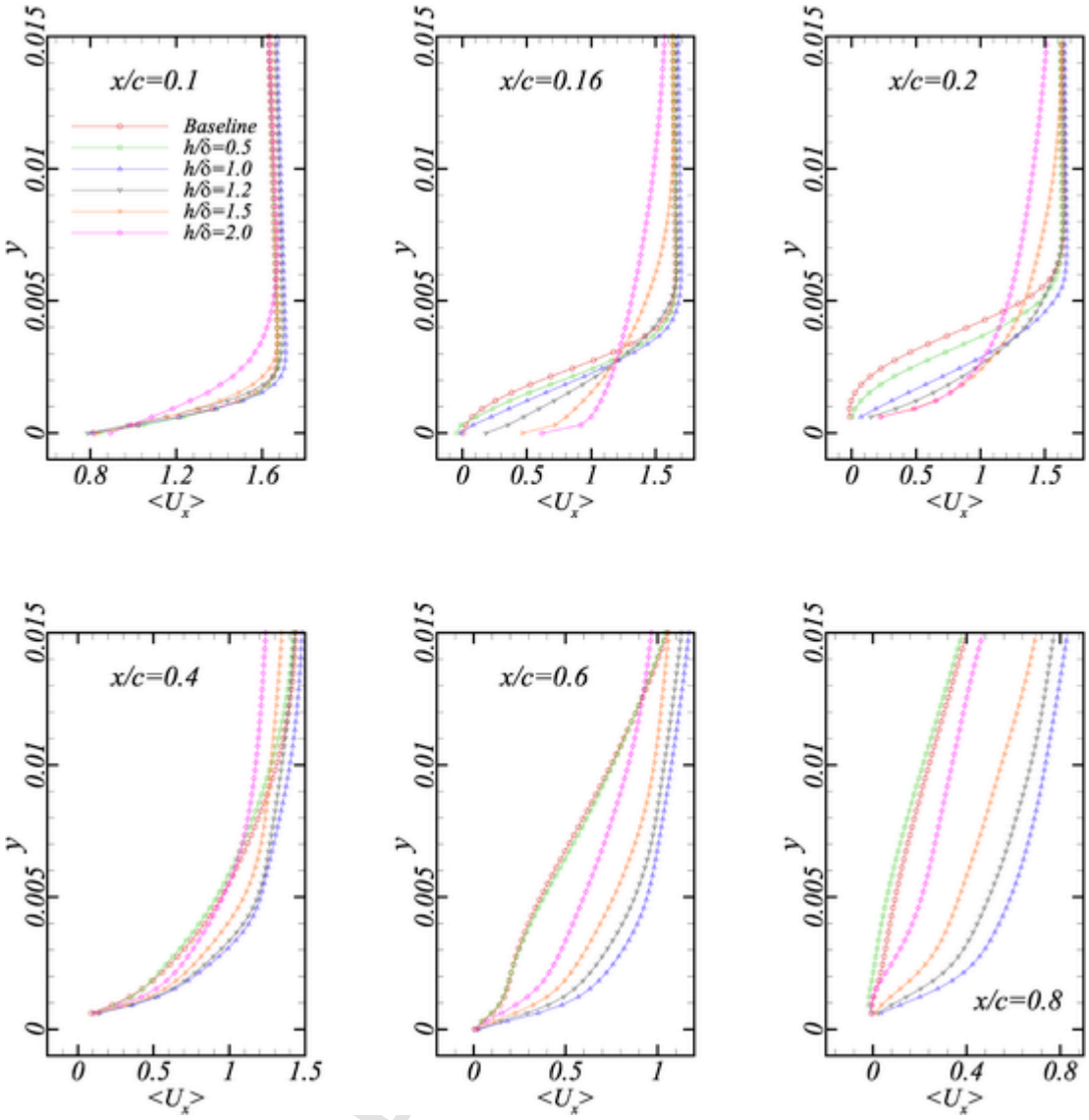

Fig. 9. Boundary layer velocity profile for five different recess depths ratio h/δ compared to the baseline condition (no grooves). The groove has an aspect ratio $h/w = 0.1$ and arc crossprofile.

over, moving the groove endpoint would produce the effect of reducing recess depth ratio (moving downstream), or increasing recess depth ratio (moving upstream) as demonstrated by the comparison between the $\Delta C_l/C_d$ results in Figs. 7 and 12.

3.5. Effect of surface grooves on the service performance of SWTs

The blade element method (BEM) is frequently used to design SWT rotor blades. Aerodynamic performance is the fundamental design consideration (Hansen, 2015). The aerodynamic lift and drag produced by the airfoil section resolve into the thrust that drives the rotor to generate power. Therefore, an airfoil section with a high lift-to-drag ratio is responsible for efficient turbine power generation.

To evaluate the effect of surface grooves on airfoil aerodynamics and service performance of SWTs, the lift and drag coefficients of a NACA 4415 airfoil with and without surface grooves at $Re_c = 2 \times 10^5$ were simulated at the *AOAs* ranging from 0° to the stall angle 18° (Fig. 14). The power coefficient C_{po} of a simplified horizontal-axis SWT using the airfoil was then calculated as a function of the blade tip speed ratio λ using the BEM (Fig. 15). The surface groove in the simulation was a rec groove with the optimum geometry and position ($h/\delta = 1.2$, $h/w = 0.15$ and $x/c = 0.16$). The predicted lift and drag coefficients were input to the BEM calculation. The lift and drag data beyond stalling was extrapolated using the Viterna equations (Viterna and Janetzke, 1982). The SWT was based on a Bergey Excel 10 wind turbine and has three blades with constant airfoil chord length (0.3 m) but no twist. The rotor diameter was 7.0 m. The BEM procedure with relevant equations used in this study was detailed in the reference (Hansen, 2015; Manwell et al., 2009).

Compared to the baseline airfoil (no grooves), the lift increases and the drag decreases at almost all the *AOAs* before stalling, especially those near the design $AOA = 10°$ (Fig. 14). This suggests that surface grooves improve the airfoil aerodynamic performance at the *AOAs* near the design point and have no negative effect at other *AOAs*. For the SWT with the baseline airfoil, the maximum power coefficient $C_{po} = 0.370$ occurs at the tip speed ratio $\lambda = 6$ (Fig. 15). The maximum $C_{po} = 0.377$ also occurs at $\lambda = 6$ for the SWT with surface grooves on the airfoil. Therefore, the power extraction of the SWT improves by 2% if grooves with the optimum features are introduced on the airfoil surface. The overall service performance enhances around the tip speed ra-

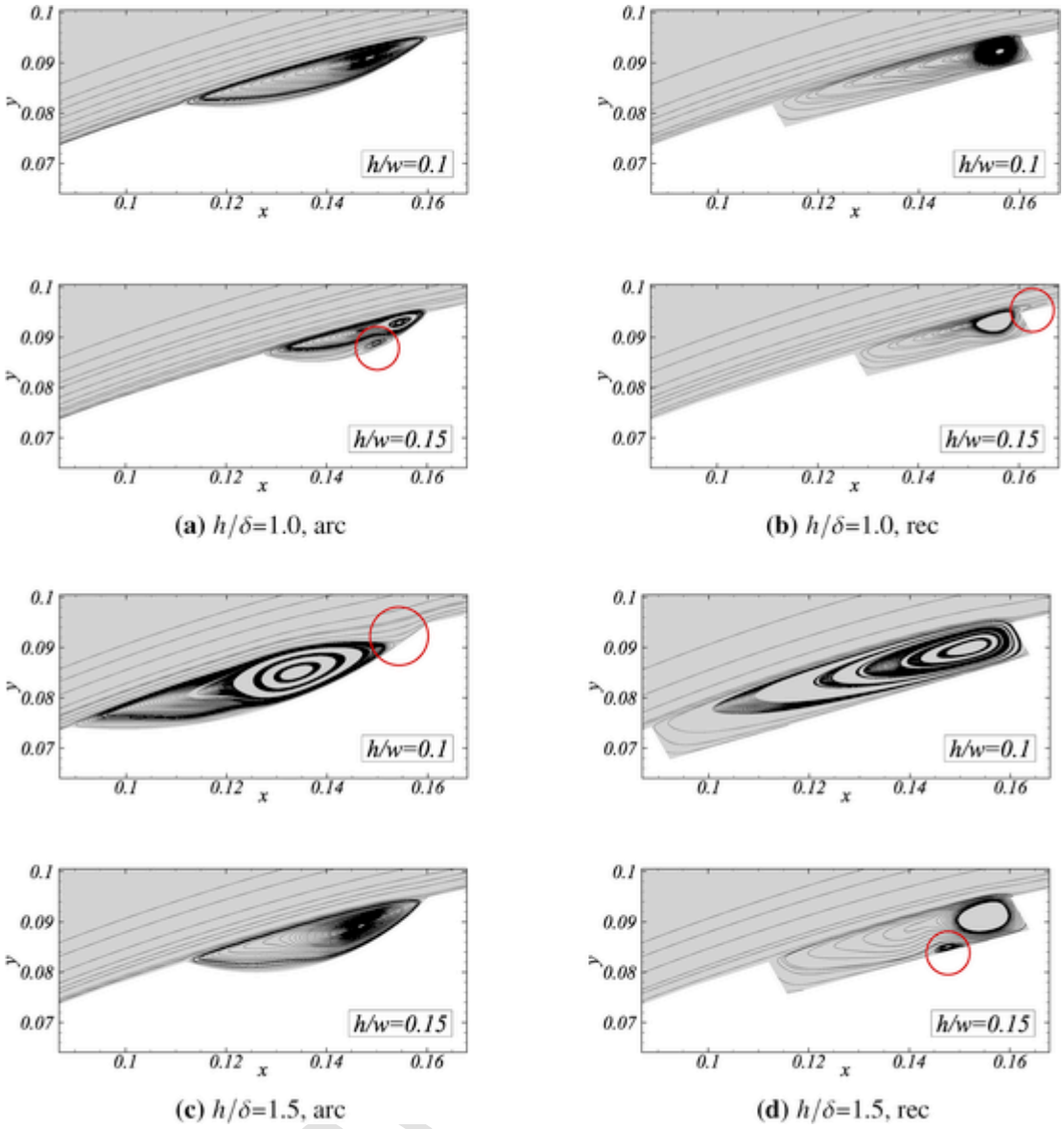

Fig. 10. Mean streamlines inside the groove for different aspect ratios h/w. The circle indicates the unstable behavior of the vortex.

tio $\lambda = 6$ (Fig. 15). At lower or higher λ, the C_{po} nearly coincides with the baseline airfoil configuration. Surface grooves with the optimum geometry/position increase the aerodynamic lift-to-drag ratio by approximately 50% at the design $AOA = 10°$ (Fig. 7), and consequently improve the power coefficient of the SWT by 2%.

Furthermore, the unsteady structural load experienced by the blade due to vortex shedding in low Reynolds number flow can be reduced as the groove can eliminate LSBs. This is beneficial to reduce part of fatigue loads applied to the blade, and potentially decrease the design weight of the blade.

4. Conclusions

The 2D flow around a NACA 4415 airfoil was simulated with the three-equation $k - k_l - \omega$ turbulence model at Reynolds number based on chord $Re_c = 2 \times 10^5$ and angle of attack $AOA = 10°$. The model was validated by the experimental data in the literature. Surface grooves were proposed to eliminate the LSBs formed on the suction surface that results in unsteady vortex shedding. A parametric simulation was performed to investigate the effect of groove characteristics including recess depth, aspect ratio, crossprofile and groove position on the aerodynamic performance. The conclusions are drawn as follows.

The key factor influencing the airfoil performance is the ratio of the recess depth to the baseline boundary layer thickness. The most effective recess depth ratio ranges from 1.0 to 1.5. The impact of the groove aspect ratio is dependent on the recess depth. A smaller aspect ratio (wider groove) can better trap the vortex for a recess depth ratio less than 1.2; but a higher aspect ratio (narrow groove) is required to stabilize the vortex if the groove is deep. Compared to an arc groove, a rectangular crossprofile in particular for a recess depth ratio 1.2–1.5 better restricts the fluid motion inside the groove, enhances the vortex stability and reduces the wall friction. Moving the groove endpoint downstream or upstream affects the potential vortex size within the groove, and produces the effect of reducing or increasing the recess depth ratio, respectively. An optimum endpoint for a rectangular groove is located at 0.16 times chord length for an aspect ratio of 0.15. Airfoil surface grooves with optimum parameters that improve the aerodynamic lift-to-drag ratio by approximately 50% at the design $AOA = 10°$ increases the power coefficient of the SWT by 2%.

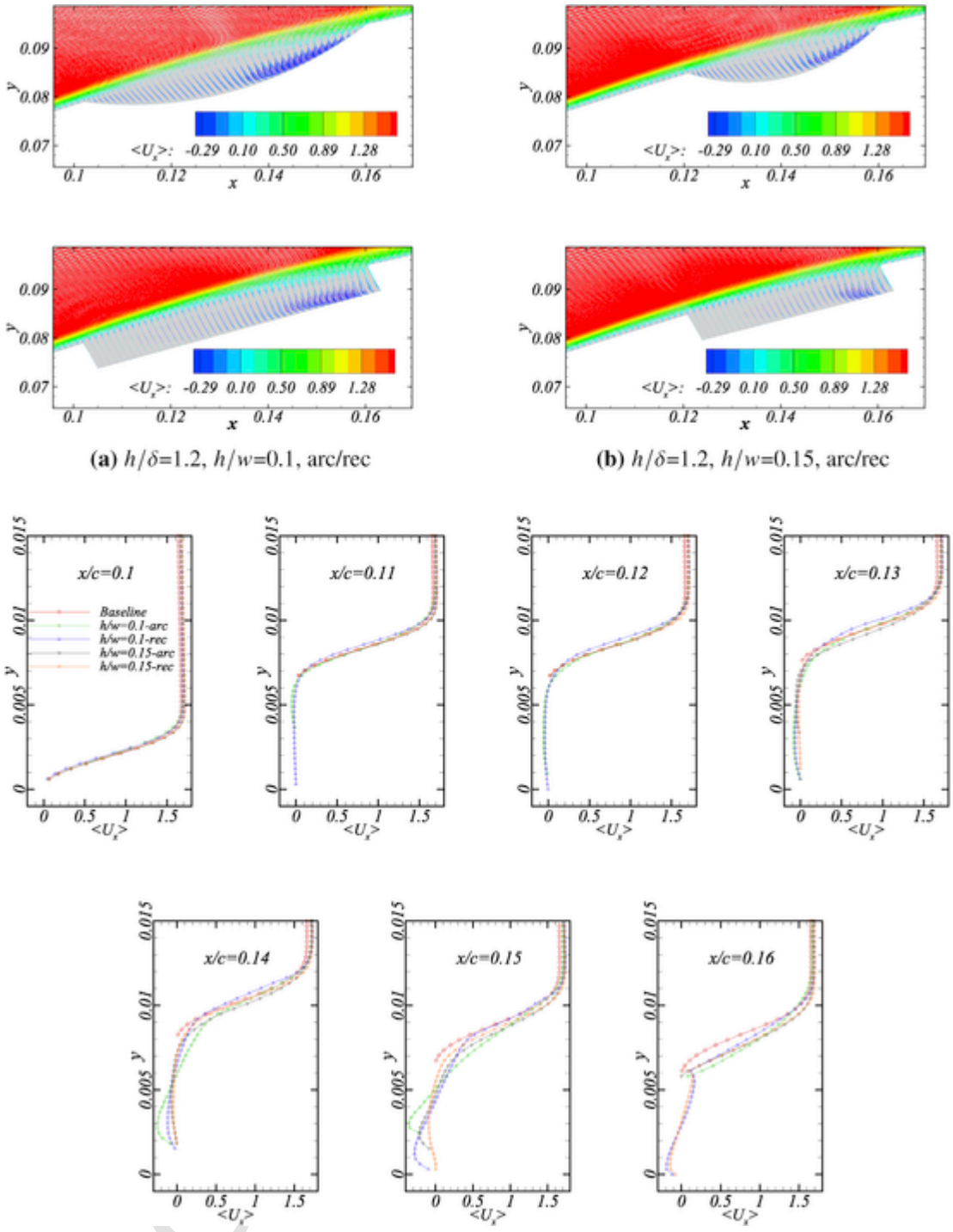

Fig. 11. The effect of groove crossprofile on mean velocity vector and boundary layer velocity profile in the groove.

CRediT authorship contribution statement

Yue Liu: Conceptualization, Methodology, Software, Validation, Formal analysis, Visualization, Investigation, Writing - original draft. **Peifeng Li:** Writing - review & editing, Supervision, Resources. **Wei He:** Investigation, Writing - review & editing. **Kaiyong Jiang:** Conceptualization, Supervision, Resources, Funding acquisition.

CRediT authorship contribution statement

Yue Liu: Conceptualization, Methodology, Software, Validation, Formal analysis, Visualization, Investigation, Writing - original draft. **Peifeng Li:** Writing - review & editing, Supervision, Resources. **Wei He:** Investigation, Writing - review & editing. **Kaiyong Jiang:** Conceptualization, Supervision, Resources, Funding acquisition.

Declaration of competing interest

The authors declare that they have no known competing financial interests or personal relationships that could have appeared to influence the work reported in this paper.

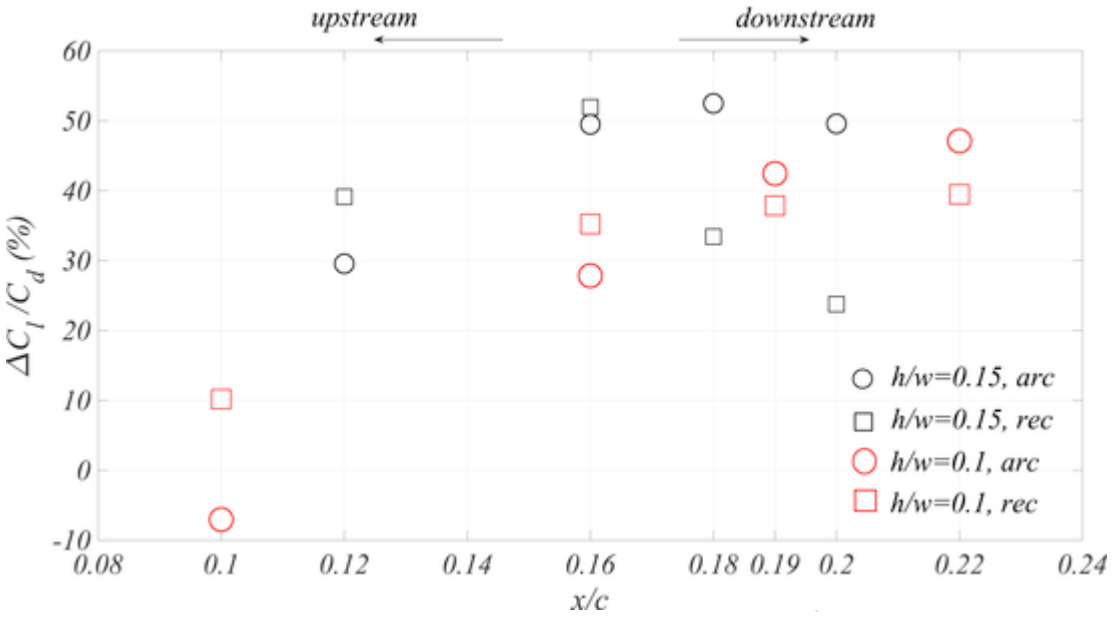

Fig. 12. The effect of the groove end position on the relative lift-to-drag ratio. The groove recess depth ratio is $h/\delta = 1.2$.

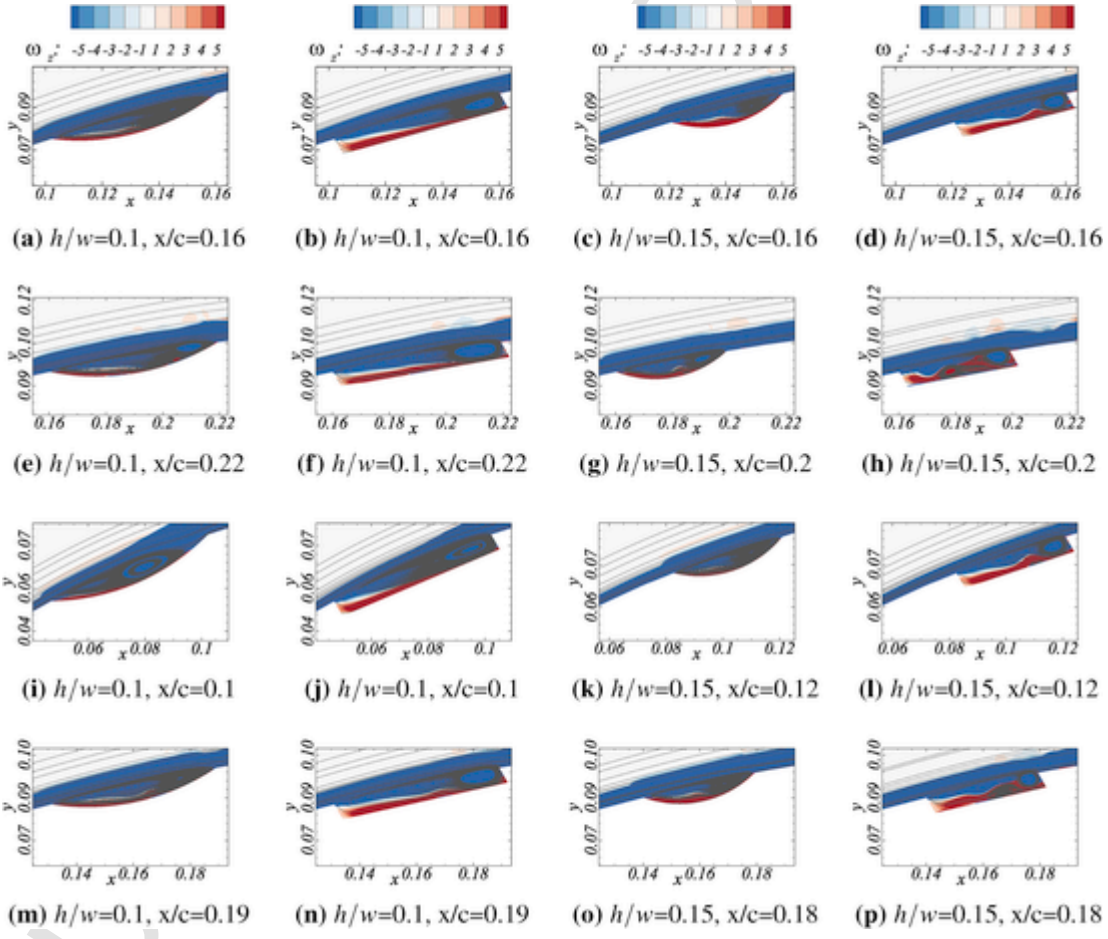

Fig. 13. Effect of groove position on the vorticity distribution inside the groove. The recess depth ratio is fixed at $h/\delta = 1.2$.

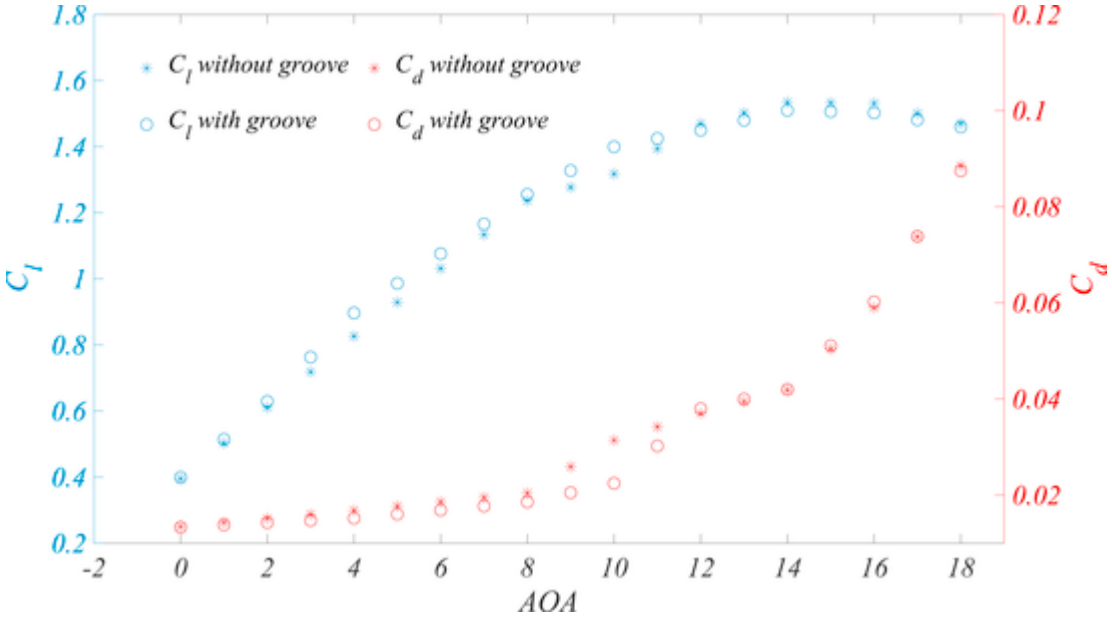

Fig. 14. Comparison of predicted lift and drag coefficients of a NACA 4415 airfoil with and without surface grooves.

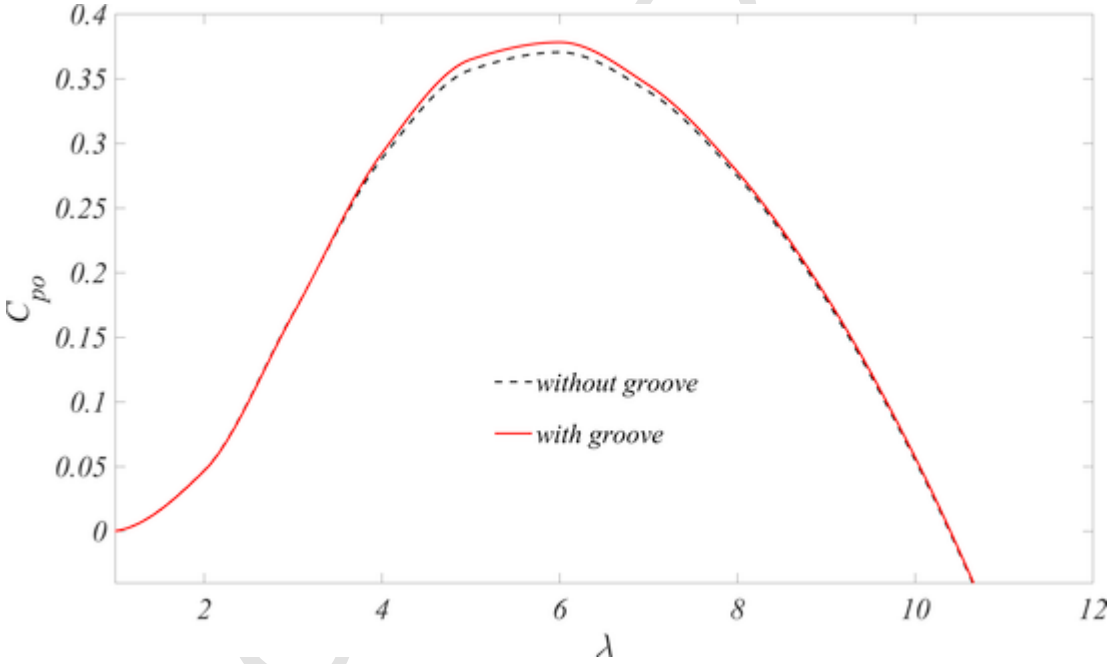

Fig. 15. Predicted power coefficient C_{po} of a SWT with and without surface grooves as a function of blade tip speed ratio λ.

Acknowledgments

The authors acknowledge the financial support of the National Natural Science Foundation of China (51475174). YL thanks the Huaqiao University International Cultivation Program for Outstanding Postgraduates.

References

Alam, F, Steiner, T, Chowdhury, H, Moria, H, Khan, I, Aldawi, F, Subic, A, 2011. A study of golf ball aerodynamic drag. Procedia Engineering 13, 226–231.

Bukala, J, Damaziak, K, Kroszczynski, K, Krzeszowiec, M, Malachowski, J, 2015. Investigation of parameters influencing the efficiency of small wind turbines. J. Wind Eng. Ind. Aerod. 146, 29–38.

Choudhry, A, Arjomandi, M, Kelso, R, 2015. A study of long separation bubble on thick airfoils and its consequent effects. Int. J. Heat Fluid Flow 52, 84–96.

Davies, J M, 1949. The aerodynamics of golf balls. J. Appl. Phys. 20 (9), 821–828.

Devinant, P, Laverne, T, Hureau, J, 2002. Experimental study of wind-turbine airfoil aerodynamics in high turbulence. J. Wind Eng. Ind. Aerod. 90, 689–707.

Fürst, J, Příhoda, J, Straka, P, 2013. Numerical simulation of transitional flows. Computing 95 (Suppl. 1), S163–S182.

Gad-el-Hak, M, 1990. Control of low-speed airfoil aerodynamics. AIAA J. 28 (9), 1537–1552.

Hansen, M O L, 2015. Aerodynamics of Wind Turbines. third ed. London and New York.

Jamieson, P, Bowles, A, Derrick, A, Leithead, W, Rogers, M, 1992. Innovative concepts for aerodynamic control of wind turbine rotors. J. Wind Eng. Ind. Aerod. 39, 395–404.

Jones, G, Santer, M, Papadakis, G, 2018. Control of low Reynolds number flow around an airfoil using periodic surface morphing: a numerical study. J. Fluid Struct. 76, 95–115.

Kirk, T M, Yarusevych, S, 2017. Vortex shedding within laminar separation bubbles forming over an airfoil. Exp. Fluid 58 (43), 1–17.

Langtry, R, Gola, J, Menter, F, 2006. Predicting 2D airfoil and 3D wind turbine rotor performance using a transition model for general CFD codes. 44th AIAA Aerospace Sciences Meeting & Exhibit 1–11.

Langtry, R B, Menter, F R, 2009. Correlation-based transition modeling for unstructured parallelized computational fluid dynamics codes. AIAA J. 47 (12), 2894–2906.

Leknys, R R, Arjomandi, M, Kelso, R M, Birzer, C H, 2018. Thin airfoil load control during post-stall and large pitch angles using leading-edge trips. J. Wind Eng. Ind. Aerod. 179, 80–91.

Lin, J C M, Pauley, L L, 1996. Low-Reynolds-Number separation on an airfoil. AIAA J. 34 (8), 1570–1577.

Lin, M, Sarlak, H, 2016. A comparative study on the flow over an airfoil using transitional turbulence models. AIP Conf. Proc 1738.

Manolesos, M, Voutsinas, S G, 2015. Experimental investigation of the flow past passive vortex generators on an airfoil experiencing three-dimensional separation. J. Wind Eng. Ind. Aerod. 142, 130–148.

Manwell, J F, McGowan, J G, Rogers, A L, 2009. Wind Energy Explained: Theory, Design and Application. second ed. WILEY, Chichester.

Mayle, R, Schulz, A, 1996. The path to predicting bypass transition. In: International Gas Turbine and Aeroengine Congress & Exhibition, 1. pp. 1–8 Birmingham, UK.

McTavish, S, Feszty, D, Nitzsche, F, 2013. Evaluating Reynolds number effects in small-scale wind turbine experiments. J. Wind Eng. Ind. Aerod. 120, 81–90.

O'Meara, M, Mueller, T, 1987. Laminar separation bubble characteristics on an airfoil at low Reynolds numbers. AIAA J. 25 (8), 1033–1041.

Pacciani, R, Marconcini, M, Arnone, A, Bertini, F, 2011. An assessment of the laminar kinetic energy concept for the prediction of high-lift, low-Reynolds number cascade flows. In: Proc. Inst. Mech. Eng. Part A-J. Power Energy, 225. pp. 995–1003.

Pröbsting, S, Yarusevych, S, 2015. Laminar separation bubble development on an airfoil emitting tonal noise. J. Fluid Mech. 780, 167–191.

Reza, T Z, Mahmood, S, Amir, K, 2009. Prediction of boundary layer transition based on modeling of laminar fluctuations using RANS approach. Chin. J. Aeronaut. 22, 113–120.

Robarge, T W, Stark, A M, Min, S-k, Khalatov, A A, Byerley, A R, 2004. Design considerations for using indented surface treatments to control boundary layer separation. In: 42nd AIAA Aerospace Sciences Meeting & Exhibit. American Institute of Aeronautics and Astronautics, pp. 1–10.

Saliveros, E, 1988. The Aerodynamic Performance of the NACA-4415 Aerofoil Section at Low Reynolds Numbers. Ph.D. thesis, University of Glasgow, Glasgow, UK.

Sanders, D D, O'Brien, W F, Sondergaard, R, Polanka, M D, Rabe, D C, 2010. Predicting separation and transitional flow in turbine blades at low Reynolds numbers—Part I: development of prediction methodology. J. Turbomach. 133, 031011.

Sanders, D D, O'Brien, W F, Sondergaard, R, Polanka, M D, Rabe, D C, 2010. Predicting separation and transitional flow in turbine blades at low Reynolds numbers—Part II: the application to a highly separated turbine blade cascade geometry. J. Turbomach. 133, 031012.

Seo, S H, Hong, C H, 2016. Performance improvement of airfoils for wind blade with the groove. J. Green Energy 13 (1), 34–39.

Spalart, P R, Rumsey, C L, 2007. Effective inflow conditions for turbulence models in aerodynamic calculations. AIAA J. 45 (10), 2544–2553.

Ting, L L, 2003. Effects of dimple size and depth on golf ball aerodynamic performance. In: Proceedings of FEDSM'03 4TH ASME JSME Joint Fluids Engineering Conference Honolulu. pp. 811–817 Hawaii, USA.

Tummala, A, Velamati, R K, Sinha, D K, Indraja, V, Krishna, V H, 2016. A review on small scale wind turbines. Renew. Sustain. Energy Rev. 56, 1351–1371.

Viterna, L A, Janetzke, D C, 1982. Theoretical and Experimental Power from Large Horizontal-Axis Wind Turbines Report No. 20320-41. NASA.

Wafula, D, Wang, C, Wei, Y, Zhu, W, 2016. Experimental and numerical study of turbulence effect on aerodynamic performance of a small-scale vertical axis wind turbine. J. Wind Eng. Ind. Aerod. 157, 1–14.

Walters, D K, Cokljat, D, 2008. A three-equation eddy-viscosity model for Reynolds-averaged Navier—Stokes simulations of transitional flow. J. Fluid Eng. 130, 121401.

Wang, C, Prinn, R G, 2010. Potential climatic impacts and reliability of very large-scale wind farms. Atmos. Chem. Phys. 10, 2053–2061.

Wang, S, Wang, S, 2015. Impacts of wind energy on environment: a review. Renew. Sustain. Energy Rev. 49, 437–443.

Wauters, J, Degroote, J, 2018. On the study of transitional low-Reynolds number flows over airfoils operating at high angles of attack and their prediction using transitional turbulence models. Prog. Aeosp. Sci. 103, 52–68.

Wauters, J, Degroote, J, Vierendeels, J, 2019. Comparative study of transition models for high-angle-of-attack behavior. AIAA J. 57 (6), 1–16.

Zhang, L, Li, X, Yang, K, Xue, D, 2016. Effects of vortex generators on aerodynamic performance of thick wind turbine airfoils. J. Wind Eng. Ind. Aerod. 156, 84–92.

Zhang, Y, Sun, Z, van Zuijlen, A, van Bussel, G, 2017. Numerical simulation of transitional flow on a wind turbine airfoil with RANS-based transition model. J. Turbul. 18 (9), 879–898.